This article has been accepted for publication in a future issue of this journal, but has not been fully edited. Content may change prior to final publication. Citation information: DOI 10.1109/TPEL.2016.2602944, IEEE Transactions on Power Electronics

Analytical Investigation of Sideband Electromagnetic Vibration in Integral-Slot PMSM Drive with SVPWM Technique

Wenyi Liang, Patrick Chi-Kwong Luk, *Senior Member, IEEE,* and Weizhong Fei, *Member, IEEE,*

***Abstract*— This paper provides a comprehensive investigation into the electromagnetic vibration associated with the sideband harmonic components introduced by space vector pulse width modulation applied in integral-slot permanent magnet synchronous machine drives. The critical permanent magnet, armature reaction, and sideband magnetic field components, which are the primary causes for sideband electromagnetic vibration in integral-slot permanent magnet synchronous machines, are identified. The analytical derivations of the magnetic field components are carried out, and amplitudes and frequencies of the resultant sideband radial electromagnetic force components are obtained. Furthermore, the proposed models of the sideband radial electromagnetic force components are incorporated into the vibration model to analytically evaluate the corresponding sideband electromagnetic vibrations of the machine. Experimental tests on an integral-slot permanent magnet synchronous machine drive are comprehensively performed to confirm the validity and accuracy of the analytical models. Not only can the validated analytical models offer insightful details in understanding the impacts of the key factors, such as operation conditions, machine geometry, electromagnetic and power converter parameters, on the sideband electromagnetic vibration, but also can be readily extended to assess and reduce noise in integral-slot permanent magnet synchronous machine drives.**

***Index Terms*—Electromagnetic vibration, integral-slot, permanent magnet synchronous machine, radial force, sideband harmonic, space vector pulse width modulation, variable speed drives.**

NOMENCLATURE

b_d, b_q	The d- and q-axis magnetic field components.
D_i	The inner diameter of stator.
δ	The torque angle.
f_r, b_r	The PM provided MMF and magnetic field.
f_s, b_s	The current provided MMF and magnetic field.
f_μ, b_μ	The sideband MMF and magnetic field.
i_d, i_q	d- and q-axis components of stator current.
K_{dp}	The fundamental winding coefficient.
L_{ad}, L_{aq}	d- and q-axis inductance components contributed only by the p^{th} spatial harmonic.
L_d, L_q	d and q inductance components.
L_{ef}	Effective length of machine.
Λ_0	The average air gap permeance.
$\bar{\Lambda}_r, \bar{\Lambda}_s$	The relative rotor saliency and slot permeance.
M	The modulation ratio.
μ_0	Permeability of vacuum.
N	Number of turns in series per phase.
ω_1	Electrical angular speed of machine.
ω_m	Natural angular frequency of the stator system for m^{th} spatial mode.
ω_s	Carrier angular speed.
p	Pole pair number of machine.
p_r	The radial force density.
ψ_f	Flux linkage of permanent magnet.
ψ_{md}, ψ_{mq}	d and q fundamental armature reaction flux linkages.
θ	The mechanical angle.
θ_1	The initial phase of fundamental current.
τ_p	Pole arc distance of p-order component.
U_{dc}	The direct current bus voltage.
Z	Stator slot number of machine.

Manuscript received April 30, 2015; revised July 10, 2016; accepted August 10, 2016. The work is supported by the Engineering and Physics Science Research Council, U.K., under Grants Ref.EP/I038543/1 and Ref.EP/L001063/1. (Corresponding author: Patrick Chi-Kwong Luk.)

The authors are with the Centre of Power Engineering, Cranfield University, Cranfield, MK43 0AL, U.K. (e-mail:w.liang@cranfield.ac.uk, p.c.k.luk@cranfield.ac.uk, w.fei@cranfield.ac.uk).

I. INTRODUCTION

EVER-INCREASING demands on electric machine drives with high performance and easy fabrication in various existing and emerging applications are reviving the research interests in permanent magnet synchronous machines (PMSMs) [1], which possess various distinctive advantages such as high torque density, great efficiency, compact structure, and fast dynamic response [2]. In general, PMSMs can be classified according to the number of slots per pole per phase: integral-slot and fractional-slot configurations. The integral-slot designs have long been a preferred choice with PMSM drive designers due to the high winding factor and simple layout. However, electromagnetic vibration, as one of the parasitic effects, is always of significant concern throughout the design and operation stages of the PMSM drive. Such vibration is attributed to the electromagnetic forces acting upon the stator and rotor cores which are induced by the air-gap magnetic field. There are generally two approaches to analyze electromagnetic forces and their related vibration in PMSMs: numerical and analytical. The electromagnetic forces can be divided into radial and circumferential ones in conventional radial-flux PMSM, which are associated with the forced radial and torsional vibrations, respectively. It is noteworthy that the electromagnetic torque is the manifestation of the circumferential ones in radial-flux machine. The investigation and

This article has been accepted for publication in a future issue of this journal, but has not been fully edited. Content may change prior to final publication. Citation information: DOI 10.1109/TPEL.2016.2602944, IEEE Transactions on Power Electronics

minimization of cogging torque and torque ripple [3]–[7] and their resultant torsional vibration [8]–[10] in PMSMs using analytical and numerical methods have been well covered. Meanwhile, the characteristics of radial electromagnetic force [11]–[14] and vibration [15]–[17] have also been extensively studied by analytical and numerical approaches.

The aforementioned studies typically only focus on the electromagnetic forces and vibrations associated with the low frequency air-gap magnetic fields, which are contributed by the permanent magnets (PMs) and low-order current harmonic components. Meanwhile, space vector pulsewidth modulation (SVPWM) technique has been rountinely implemented to achieve excellent steady-state and dynamic performances in PMSM drives. However, SVPWM technique will inevitably generate sideband harmonic components, whose frequencies are generally located nearby the carrier frequency and its multiples, during the intrinsic switching process. The sideband harmonic components will generate high frequency harmonic magnetic fields which become one of the main causes of high-frequency electromagnetic vibration and noise in PMSM drives. As the amplitudes of the sideband harmonic components are relatively small, the resultant sideband electromagnetic torque ripple will be trivial compared with the low-frequency ones. Despite the small amplitudes of the sideband radial electromagnetic forces, the corresponding high frequencies are sometimes much closer to the natural resonance frequencies of the radial vibration modes and hence susceptible to high radial electromagnetic vibration and importantly severe ear-piercing acoustic noise. Consequently, the sideband harmonic magnetic fields and the associated high frequency radial electromagnetic forces are of particular importance for electromagnetic vibration analysis in PMSM drives. The high-frequency sideband electromagnetic vibration generated by SVPWM technique is distinguished from that close to the fundamental electrical frequency. The unpleasant high-frequency electromagnetic noise associated with such sideband electromagnetic vibration is quite a common issue in many different applications, such as electric propulsions and elevators.

However, the literature on high-frequency electromagnetic vibration and acoustic noise related to pulsewidth modulation (PWM) techniques is very limited. Novel PWM techniques which employ trapezoidal modulator with fixed [18], variable frequency triangular [19], and sinusoidal [20] carrier signal, as well as random switching frequency [21], [22], have been proposed and investigated in order to reduce the acoustic noise in the drives. Moreover, a simplistic switching frequency strategy is implemented to avoid close proximity to the natural frequencies for vibration and noise reduction [23]. However, evident audible noise can still occur even though the excitation frequencies are far away from the natural ones. Thus, it is proposed that an active filter is introduced between the voltage source inverter (VSI) and induction machine to improve the acoustic behavior [24]. Nonetheless, those studies are all carried out for induction machine drives and unlikely to be applicable for PMSM ones as the mechanism of electromagnetic flux generation is different.

There is a dearth of research on sideband electromagnetic vibration and acoustic noise originated from SVPWM technique, especially in PMSM drives. As SVPWM carrier frequency is normally two orders of magnitude higher than the electrical frequency of the machine, excessively small time steps are essential for numerical simulation to accurately predict the sideband harmonic components. This makes the finite element analysis (FEA) approach computationally extremely demanding and no longer practical for the sideband electromagnetic vibration evaluation. Therefore, it is of particular importance to develop fast yet effective analytical methods for sideband harmonic components. Not until quite recently have there been focused investigations on full direct analytical developments of sideband voltage and current harmonic components in the induction machine [25] and PMSM [26] drive systems with SVPWM technique. This paper extends from the analytical sideband current harmonic model [26] to the corresponding radial electromagnetic force density and hence vibration derivations in integral-slot PMSM drives. In order to derive the analytical expressions for the radial electromagnetic forces, it is particularly important to decompose the air-gap magnetic field into the key radial and circumferential components. The air-gap magnetic field components,contributed by permanent magnet, low-frequency armature current components, and high-frequency sideband current harmonics, are first revealed and investigated. The critical permanent magnet, armature reaction, and sideband magnetic field components, which are primarily responsible for the sideband electromagnetic vibration in integral-slot PMSM drive, are then identified and analytically obtained, and followed by the analytical derivations of the amplitudes and frequencies of the resultant critical sideband radial electromagnetic force components. Furthermore, the proposed models of the sideband radial electromagnetic force components are incorporated into the vibration model to analytically evaluate the corresponding electromagnetic vibrations of the machine. Finally, comprehensive experimental tests on an prototype integral-slot PMSM drive are carried out and the broadly close agreements between the analytical and experimental results have confirmed the accuracy and validity of the analytical models. The factors which affect the sideband radial electromagnetic force density, such as electrical parameters, control strategy, power converter parameters, and operational condition, have all been taken into considerations during the analytical derivations. Therefore, not only can the proposed analytical approach promptly assess the sideband electromagnetic vibration during the design stage of integral-slot PMSM drive with SVPWM technique, but also serve as an effective tool for minimization during optimization stage.

II. Low-frequency air-gap magnetic field

Generally, the interactions between the PM and low-frequency armature magnetomotive forces (MMFs), together with air-gap variation due to slot openings and rotor saliency effects, will result in abundant low-frequency magnetic field components in the air gap of integral-slot PMSMs. Therefore, it is of particular importance to reveal those components and identify the critical ones for sideband electromagnetic

This article has been accepted for publication in a future issue of this journal, but has not been fully edited. Content may change prior to final publication. Citation information: DOI 10.1109/TPEL.2016.2602944, IEEE Transactions on Power Electronics

vibration study. In order to obtain the analytical expressions of the magnetic field, it is assumed that the superposition principle of the magnetic field is valid.

A. PM Magnetic Field

It is assumed that the rotation direction of the fundamental, the p^{th}-order magnetic field is defined as positive. Then the MMF provided by PMs can be presented as

$$f_r(\theta,t)=\sum_{\upsilon} F_{r\upsilon}\cos(\upsilon p\theta-\upsilon\omega_1 t) \tag{1}$$

where $\upsilon=2k-1, k=1,2,\cdots$. By taking the slot opening and rotor saliency effects into account, the air gap permeance distribution can be expressed as

$$\lambda(\theta,t)=\Lambda_0\cdot\bar{\Lambda}_r(\theta,t)\cdot\bar{\Lambda}_s(\theta,t) \tag{2}$$

where

$$\begin{cases}\bar{\Lambda}_r(\theta,t)=\sum_{m=0}^{\infty}\dfrac{\Lambda_{2m}}{\Lambda_0}\cos\left(2mp\theta-2m\omega_1 t\right)\\ \bar{\Lambda}_s(\theta,t)=\sum_{n=0}^{\infty}\dfrac{\Lambda_{nZ}}{\Lambda_0}\cos\left(nZ\theta\right)\end{cases} \tag{3}$$

The PM magnetic field in the air gap can be derived by applying Hopkinson's law as

$$b_r(\theta,t)=f_r(\theta,t)\cdot\lambda(\theta,t) \tag{4}$$

By substituting equations (1) and (3) into (4), all the magnetic field components with different spatial orders and frequencies can be obtained accordingly. The flux density in equation (4) can be divided into two parts: slotless components and slot harmonic components. The slotless ones can be expressed as $f_r\Lambda_0\bar{\Lambda}_r$ and presented as

$$b_{r_1}(\theta,t)=\sum_{\upsilon} B_{r\upsilon}\cos(\upsilon p\theta-\upsilon\omega_1 t) \tag{5}$$

where

$$B_{r\upsilon}=\sum_{m\geq 0}\frac{F_{r(\upsilon+2m)}\Lambda_{2m}}{2}+\sum_{2m<\upsilon}\frac{F_{r(\upsilon-2m)}\Lambda_{2m}}{2}+\sum_{2m>\upsilon}\frac{F_{r(2m-\upsilon)}\Lambda_{2m}}{2} \tag{6}$$

Particularly, the fundamental component can be expressed as

$$B_{r1}=F_{r1}\Lambda_0+\sum_{m\geq 1}\frac{(F_{r(2m-1)}+F_{r(2m+1)})\Lambda_{2m}}{2} \tag{7}$$

On the other hand, the slot harmonic components can be expressed as

$$b_{r_2}(\theta,t)=\sum_{\upsilon}\sum_{n} B_{r\upsilon n}\cos\left((\upsilon p\pm nZ)\theta-\upsilon\omega_1 t\right) \tag{8}$$

where $B_{r\upsilon n}$ is presented as

$$B_{r\upsilon n}=\frac{B_{r\upsilon}\Lambda_{nZ}}{2\Lambda_0} \tag{9}$$

Thus, the magnetic field components contributed by PMs are derived and given in Table I. Generally, the fundamental component is the main one for most of the cases.

TABLE I
LOW-FREQUENCY AIR-GAP MAGNETIC FIELD COMPONENTS

No.	Spatial Order	Frequency	Amplitude
1	p	ω_1	B_{r1}
2	p	ω_1	B_{s1}
3	υp	$\upsilon\omega_1$	$B_{r\upsilon}$
4	$(\kappa\pm 2m)p$	$(\nu\pm 2m)\omega_1$	$B_{s\nu\kappa m}$
5	$\upsilon p\pm nZ$	$\upsilon\omega_1$	$B_{r\upsilon n}$
6	$(\kappa\pm 2m)p\pm nZ$	$(\nu\pm 2m)\omega_1$	$B_{s\nu\kappa mn}$

B. Low-Frequency Armature Reaction Magnetic Field

The MMF provided by low-frequency current armature reaction can be expressed as

$$f_s(\theta,t)=\sum_{\nu}\sum_{\kappa} F_{s\nu\kappa}\cos(\kappa p\theta-\nu\omega_1 t-\theta_\nu) \tag{10}$$

where ν=$\pm 6k+1$, k=$0,1,2,\cdots$ refers to the corresponding low-frequency current harmonics, especially ν=1 represents the fundamental one, while κ is related to the winding arrangement. In integral-slot PMSM, for single layer integral slot machine, κ are $(\pm 3k+1)p$ and $(\pm 6k+1)p$, k=$0,1,2,\ldots$, for single-layer and double-layer windings, respectively.

Similarly, the low-frequency armature reaction magnetic field components can be derived by applying Hopkinson's law as

$$b_s(\theta,t)=f_s(\theta,t)\cdot\lambda(\theta,t) \tag{11}$$

They can also be divided into slotless and slotted ones. The slotless ones can be derived and written as

$$b_{s_1}(\theta,t)=\sum_{\nu}\sum_{\kappa}\sum_{r} B_{s\nu\kappa m}\cos((\kappa\pm 2m)p\theta-(\nu\pm 2m)\omega_1 t-\theta_\nu) \tag{12}$$

where

$$B_{s\nu\kappa m}=\frac{F_{s\nu\kappa}\Lambda_{2m}}{2} \tag{13}$$

By neglecting the armature reaction of harmonic currents, the fundamental magnetic field can be simplified as

$$b_{s1}(\theta,t)\simeq F_{s(\nu=\kappa=1)}\Lambda_0\cos(p\theta-\omega_1 t-\theta_1)+F_{s(\nu=\kappa=1)}\frac{\Lambda_2}{2}\cos(p\theta-\omega_1 t+\theta_1) \tag{14}$$

where, $\theta_1=\pi/2-\arctan(i_d/i_q)$. On the other hand, the slotted ones can be expressed as

$$b_{s_2}(\theta,t)=\sum_{\nu}\sum_{\kappa}\sum_{m}\sum_{n} B_{s\nu\kappa mn}\cos(((\kappa\pm 2m)p\pm nZ)\theta-(\nu\pm 2m)\omega_1 t-\theta_\nu) \tag{15}$$

where

$$B_{s\nu\kappa rn}=\frac{F_{s\nu\kappa}\Lambda_{2m}\Lambda_{nZ}}{4} \tag{16}$$

All the magnetic field components induced by low-frequency armature reaction are obtained and given in Table I accordingly.

This article has been accepted for publication in a future issue of this journal, but has not been fully edited. Content may change prior to final publication. Citation information: DOI 10.1109/TPEL.2016.2602944, IEEE Transactions on Power Electronics

C. Analytical Model of Critical Components

The fundamental component, first item in Table I, is normally designed as the primary one to optimize the overall performance of integral-slot PMSM drive. On the other hand, the fundamental component of the armature current is the dominant one in PMSM drive with SVPWM technique, while the integral-slot configuration makes the p^{th} spatial order component much larger than the higher order ones. Therefore, the p^{th} spatial order component generated by the fundamental current component, second item in Table I, is the major one from the low-frequency armature reaction in integral-slot PMSM drive. Obviously, these two main components have the same spatial order and electrical frequency, thus they can be synthesized by superposition principle as the critical air-gap magnetic field components in integral-slot PMSM, which will interact with the critical sideband ones to generate sideband electromagnetic vibration. Without loss of generality, the analytical derivation in d-q model of this critical air-gap magnetic field component is carried out here.

The air-gap flux linkages related to the critical magnetic field component in d- and q-axes of integral-slot PMSM can be approximately expressed as

$$\psi_{md} = L_{ad} i_d + \psi_f, \psi_{mq} = L_{aq} i_q \tag{17}$$

where the d- and q-axis inductances are the component contributed only by the p^{th} spatial harmonic component in the machine. As the d-axis is the position reference for the air-gap magnetic field, and the expressions of the critical magnetic field component can be derived accordingly as

$$b_d = \frac{(L_{ad} i_d + \psi_f)\cos(p\theta)}{\alpha \tau_p N K_{dp} L_{ef}}, b_q = \frac{L_{aq} i_q \sin(p\theta)}{\alpha \tau_p N K_{dp} L_{ef}} \tag{18}$$

where α can be approximated as $2/\pi$. With the superposition principle, the critical air-gap magnetic field component can be synthesized as

$$b_0(\theta, t) = B_0 \cos(p\theta - \theta_0) \tag{19}$$

where

$$\begin{cases} B_0 = \dfrac{\sqrt{(L_{ad} i_d + \psi_f)^2 + (L_{aq} i_q)^2}}{\alpha \tau_p N K_{dp} L_{ef}} \\ \theta_0 = \arctan \dfrac{L_{aq} i_q}{L_{ad} i_d + \psi_f} \end{cases} \tag{20}$$

By neglecting the voltage drop of the winding resistances, $\theta_0 \simeq \delta$ can be obtained. It can be presented in the stator stationary reference frame as

$$b_0(\theta, t) = B_0 \cos(p\theta - \omega_1 t - \delta) \tag{21}$$

However, the nonlinearity of ferromagnetic material will inevitably bring about magnetic saturation in the PMSMs under heavy load operations. This will result in interactions between the magnetic field components from the PMs and armature reaction so that the normal superposition principle is no longer valid and applicable. Consequently, the parameters, such as L_{ad}, L_{aq}, and ψ_f, are current-dependent and can be accurately evaluated by FEA with frozen permeability technique.

TABLE II
SIDEBAND AIR-GAP MAGNETIC FIELD COMPONENTS

No.	Spatial Order	Frequency	Amplitude
1	p	ω_μ	$B_{\mu 1}$
2	$(\kappa \pm 2m)p$	$\omega_\mu \pm 2m\omega_1$	$B_{\mu\kappa m}$
3	$(\kappa \pm 2m)p \pm nZ$	$\omega_\mu \pm 2m\omega_1$	$B_{\mu\kappa mn}$

III. SIDEBAND AIR-GAP MAGNETIC FIELD

The SVPWM technique will generate clusters of sideband voltage and current harmonic components near integral multiples of the switching frequency in the stator windings of the integral-slot PMSMs. These sideband current harmonic components will induce numerous high-frequency sideband magnetic field components in the machine. Thus, it is essential to identify the critical sideband current harmonic components and their associated key magnetic field components for sideband electromagnetic vibration in integral-slot PMSM drives.

A. Sideband Armature Reaction Magnetic Field

Resembling the low-frequency current armature reaction, the μ-order sideband current induced MMF can be presented as

$$f_\mu(\theta, t) = \sum_{k=0}^{\infty} F_{\mu\kappa} \cos(\omega_\mu t - \kappa p\theta - \theta_\mu) \tag{22}$$

Analogously, the corresponding air-gap magnetic field components can be expressed as

$$b_\mu(\theta, t) = f_\mu(\theta, t) \cdot \lambda(\theta, t) \tag{23}$$

and the respective slotless and slotted ones can be obtained as

$$b_{\mu_1}(\theta, t) = \sum_{\kappa} \sum_{m} B_{\mu\kappa m} \cos((\omega_\mu \pm 2m\omega_1)t - (\kappa \pm 2m)p\theta - \theta_\mu) \tag{24}$$

and

$$b_{\mu_2}(\theta, t) = \sum_{\kappa} \sum_{m} \sum_{n} B_{\mu\kappa mn} \cos((\omega_\mu \pm 2m\omega_1)t - ((\kappa \pm 2m)p \pm nZ)\theta - \theta_\mu) \tag{25}$$

where

$$B_{\mu 1} = F_{\mu 1}\Lambda_0, B_{\mu\kappa m} = \frac{F_{\mu\kappa}\Lambda_{2m}}{2}, \quad B_{\mu\kappa mn} = \frac{B_{\mu\kappa m}\Lambda_{nZ}}{2}. \tag{26}$$

All the magnetic field components generated by sideband armature reaction are derived and given in Table II.

B. Analytical Model of Critical Components

For certain current harmonic component, the p^{th} spatial order component of the air-gap magnetic field related is the dominant one in integral-slot PMSM. Therefore, the p^{th} spatial order component induced by the main sideband current harmonic components, first item in Table II, is the critical one. From the rotor synchronous reference frame, the $(\omega_s \pm 3\omega_1)$-

This article has been accepted for publication in a future issue of this journal, but has not been fully edited. Content may change prior to final publication. Citation information: DOI 10.1109/TPEL.2016.2602944, IEEE Transactions on Power Electronics

and $2\omega_s$-order harmonic currents are the main ones in first and second carrier frequency domains, respectively [25], [26]. Normally, the sideband harmonic components beyond the first carrier frequency domain have quite high electrical frequencies that are not sensitive to auditory. Without loss of generality, only the main components in the first carrier frequency domains are considered and expressed as [26]

$$\begin{cases} i_{d\_13} = & -\dfrac{C_{12}U_{dc}\sin(\omega_s t \pm 3\omega_1 t \mp \delta)}{2(\omega_s \pm 3\omega_1)L_d} \\ & -\dfrac{C_{14}U_{dc}\sin(\omega_s t \pm 3\omega_1 t \pm \delta)}{2(\omega_s \pm 3\omega_1)L_d} \\ i_{q\_13} = & \mp\dfrac{C_{12}U_{dc}\cos(\omega_s t \pm 3\omega_1 t \mp \delta)}{2(\omega_s \pm 3\omega_1)L_q} \\ & \pm\dfrac{C_{14}U_{dc}\cos(\omega_s t \pm 3\omega_1 t \pm \delta)}{2(\omega_s \pm 3\omega_1)L_q} \end{cases} \tag{27}$$

The detailed analytical expressions of coefficients C_{12} and C_{14} are provided in Appendix. The fundamental air-gap flux linkages (spatially p^{th} order) caused by the μ^{th} sideband current harmonic component can be expressed as

$$b_{d\mu} = \frac{L_{ad} i_{d\mu}\cos(p\theta)}{\alpha\tau_p N K_{dp} L_{ef}}, b_{q\mu} = \frac{L_{aq} i_{q\mu}\sin(p\theta)}{\alpha\tau_p N K_{dp} L_{ef}} \tag{28}$$

By substituting (27) into (28) and applying superposition principle, the corresponding sideband magnetic field can be derived and transformed into the stator stationary frame as

$$\begin{cases} b_{12} = \mp\sigma_1 B_{\mu 1} C_{12}\sin(p\theta \pm (\omega_s \pm 2\omega_1)t - \delta) \\ \qquad \mp\sigma_2 B_{\mu 1} C_{14}\sin(p\theta \pm (\omega_s \pm 2\omega_1)t + \delta) \\ b_{14} = \pm\sigma_2 B_{\mu 1} C_{12} sin(p\theta \mp (\omega_s \pm 4\omega_1)t + \delta) \\ \qquad \pm\sigma_1 B_{\mu 1} C_{14} sin(p\theta \mp (\omega_s \pm 4\omega_1)t - \delta) \end{cases} \tag{29}$$

where

$$\begin{cases} \sigma_1 = L_{ad}/L_d + L_{aq}/L_q, \sigma_2 = L_{ad}/L_d - L_{aq}/L_q \\ B_{\mu 1} = \dfrac{U_{dc}}{4\alpha\tau_p N K_{dp} L_{ef}(\omega_s \pm 3\omega_1)} \end{cases} \tag{30}$$

IV. Sideband Radial Electromagnetic Force Density and Vibration

A. Sideband Radial Electromagnetic Force Density Components

The high-frequency sideband magnetic field components in the air gap will interact with the low-frequency PM and armature reaction ones to produce high-frequency sideband radial electromagnetic force components, which are prone to high-frequency electromagnetic vibration and hence leading to unpleasant acoustic noise despite small amplitudes. The radial and circumferential components of the air-gap magnetic field are required for the calculation of the radial electromagnetic force density. Normally, the radial and circumferential counterparts will have exactly the same spatial orders and frequencies while the amplitudes of the circumferential ones are much smaller than the radial ones. For the sake of simplicity, only the radial components are considered here. Thus, the sideband radial electromagnetic force density components can be derived based on Maxwell Stress Tensor theory as

$$p_r(\theta, t) \simeq -\frac{(b_r(\theta, t) + b_s(\theta, t))b_\mu(\theta, t)}{\mu_0} \tag{31}$$

By substituting the magnetic field components in Table I and II into (31), the comprehensive list of sideband radial electromagnetic force density components can be derived. However, most of them are practically negligible due to their rather small amplitudes. As only the first sideband components considered, there are abundant components with the frequencies near ω_s which can easily reach up to several thousands or above in practice. Moreover, the PWM switching frequency ω_s is far larger than frequencies of the main components produced by PM and armature reaction, it can be considered that the frequencies of sideband radial force density are approximately equal to ω_s. It is noteworthy that the damping factors have important roles for high-frequency resonance and the resonant effects will not be as significant as in the low nature frequency cases. As a consequence, the amplitudes of the sideband radial force density is the main factor rather than the spatial order. It means the low order sideband electromagnetic vibration will not be necessarily larger than the high spatial order one for sideband components. Hence, only the critical components proposed in (21) and (29) are taken into account in the model (31) to analyze the large amplitude components. However, it is still of particular importance to analyze the sideband radial electromagnetic force density components together with the resonant frequencies of their corresponding spatial orders.

B. Analytical Model of Main Components

Based on the aforementioned critical components of both low-frequency air-gap magnetic field and high-frequency sideband one, the main sideband radial electromagnetic force density components can be analytically derived. By substituting (21) and (29) into (31), the corresponding sideband radial electromagnetic force density components , which include $2p^{th}$ and 0^{th} spatial order ones, are obtained respectively as

$$\begin{cases} p_{11} = \mp\sigma_1 C_{12} K_{p1}\sin(2p\theta \pm (\omega_s \pm \omega_1)t - 2\delta) \\ \qquad \mp\sigma_2 C_{14} K_{p1}\sin(2p\theta \pm (\omega_s \pm \omega_1)t) \\ p_{15} = \pm\sigma_1 C_{14} K_{p1}\sin(2p\theta \mp (\omega_s \pm 5\omega_1)t - 2\delta) \\ \qquad \pm\sigma_1 C_{12} K_{p1}\sin(2p\theta \mp (\omega_s \pm 5\omega_1)t) \\ p_{13} = -\sigma_1(C_{12} + C_{14})K_{p1}\sin((\omega_s \pm 3\omega_1)t) \\ \qquad -\sigma_2 C_{12} K_{p1}\sin((\omega_s \pm 3\omega_1)t \mp 2\delta) \\ \qquad -\sigma_2 C_{14} K_{p1}\sin((\omega_s \pm 3\omega_1)t \pm 2\delta) \end{cases} \tag{32}$$

where

$$K_{p1} = \frac{B_{\mu 1} B_0}{2\mu_0} \tag{33}$$

For the $2p^{th}$ spatial order components, there are generally four different frequencies of $(\omega_s \pm \omega_1)$ and $(\omega_s \pm 5\omega_1)$. The respective amplitudes of them can be evaluated as

$$\begin{cases} P_{11} = K_{p1}\sqrt{\sigma_1^2 C_{12}^2 + \sigma_2^2 C_{14}^2 + 2\sigma_1\sigma_2 C_{12} C_{14}\cos(2\delta)} \\ P_{15} = K_{p1}\sqrt{\sigma_1^2 C_{14}^2 + \sigma_2^2 C_{12}^2 + 2\sigma_1\sigma_2 C_{12} C_{14}\cos(2\delta)} \end{cases} \tag{34}$$

Meanwhile, there are two different frequencies of $(\omega_s \pm 3\omega_1)$ for the 0^{th} spatial order components. The corresponding amplitudes can be expressed as

$$P_{13} = K_{p1}\sqrt{K_{13\_1} + K_{13\_2}} \tag{35}$$

This article has been accepted for publication in a future issue of this journal, but has not been fully edited. Content may change prior to final publication. Citation information: DOI 10.1109/TPEL.2016.2602944, IEEE Transactions on Power Electronics

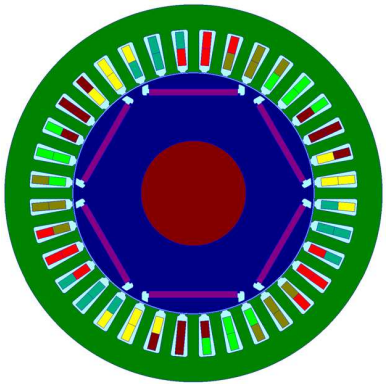

Fig. 1. The cross-section of the prototype integral-slot PMSM.

Where

$$\begin{aligned} K_{13\_1} &= (\sigma_1^2+\sigma_2^2)(C_{12}^2+C_{14}^2)+2\sigma_2^2C_{12}C_{14}\cos 4\delta \\ K_{13\_2} &= 2\sigma_1^2C_{12}C_{14}+2\sigma_1\sigma_2(C_{12}+C_{14})^2\cos 2\delta \end{aligned} \tag{36}$$

L_d and L_q in integral-slot PMSM are contributed mainly by the respective L_{ad} and L_{aq} from p^{th} spatial harmonic component, as the leakage components are relatively small and normally negligible. Hence, the amplitudes of the sideband radial electromagnetic force density components can be approximated by assuming L_d=L_{ad} and L_q=L_{aq} as

$$\begin{cases} P_{11} \simeq 2K_{p1}C_{12} \\ P_{15} \simeq 2K_{p1}C_{14} \\ P_{13} \simeq 2K_{p1}(C_{12}+C_{14}) \end{cases} \tag{37}$$

C. Sideband Electromagnetic Vibration

Based on the sideband radial electromagnetic force density models above, the amplitude of sideband electromagnetic vibration can be analytically derived as

$$A_{m\omega_\mu} = \frac{\pi D_i L_{ef} P_{m\_\omega_\mu}}{m_c\sqrt{(\omega_m^2-\omega_\mu^2)^2+4\xi_m^2\omega_\mu^2\omega_m^2}} \tag{38}$$

where $P_{m\_\omega_\mu}$ is the amplitude of m^{th} spatial order sideband radial electromagnetic force density component with frequency of ω_μ, and can be directly obtained from (34) and (35). The angular natural frequency of the stator system for m^{th} spatial order mode, ω_m, can be accurately evaluated by eigen frequency analysis in mechanical FEA software [27]. Moreover, the modal damping ratio, ξ_m, is suggested based on an empirical expression for the small-size electrical machines as [28]

$$\xi_m = \frac{1}{2\pi}(4.39\times 10^{-6}\omega_m + 0.062). \tag{39}$$

V. Experimental Validations

A. Prototype Integral-Slot PMSM Drive System

The experimental investigations on a prototype integral-slot PMSM drive system under different operational conditions are comprehensively carried out in order to validate the analytical derivations developed in the foregoing sections. PMSMs with two slots per pole per phase, which can be facilitated with two-layer overlapping windings, are widely employed for various high-performance drive systems. Therefore, the prototype integral-slot PMSM for experimental validations possesses such configuration with 6 rotor poles and 36 stator slots. The machine, whose radial cross-section is depicted as Fig. 1, is driven by a conventional two-level VSI with SVPWM technique and maximum torque per ampere (MPTA) control

TABLE III
Key Design Parameters of the Machine

Machine Parameter	Value	Machine Parameter	Value
Pole number	6	Slot number	36
Shell diameter	188mm	Shell height	220mm
Stator outer diameter	162mm	Axial stator length	129mm
Stator inner diameter	104mm	Stator yoke height	11mm
DC link voltage	280V	PWM frequency	6kHz
Rated speed	1000rpm	Maximum speed	1250rpm
Rated torque	9.5Nm	Rated power	1kW
d-axis inductance	5.8mH	q-axis inductance	18.6mH
Leakage inductance	0.24mH	Winding coefficient	0.933

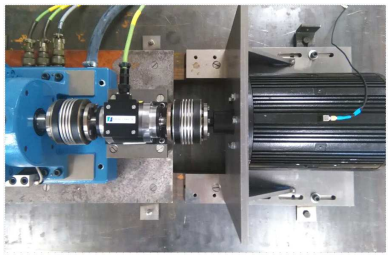

Fig. 2. The experimental setup of the PMSM drive system.

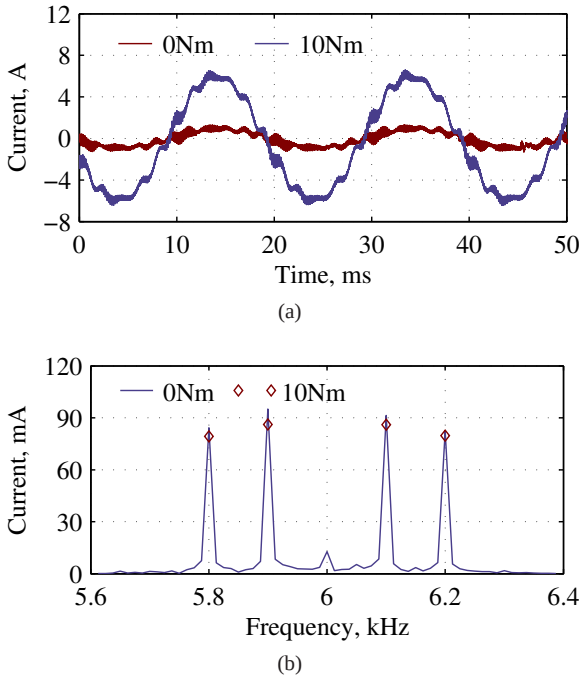

Fig. 3. Current waveform and spectrum at 1000rpm with no-load condition: (a) Current waveform, (b) Current spectrum at first carrier frequency domain.

This article has been accepted for publication in a future issue of this journal, but has not been fully edited. Content may change prior to final publication. Citation information: DOI 10.1109/TPEL.2016.2602944, IEEE Transactions on Power Electronics

strategy [29]. The main parameters of the drive system are given in Table III, and the experimental setup is shown in Fig. 2. The Dytran 3023A1 triaxial IEPE accelerometer is used to measure the radial vibration of the prototype stator during the experiment, while Soundbook Expander 908011.6 from SINUS Messtechnik GmbH is employed for data acquisition and process. The recommended measurement range of the accelerometer is from 1.5Hz to 10kHz. The specific combination of stator slot and rotor pole numbers together with the winding configuration can significantly reduce the harmful back electromotive force (EMF) harmonics, especially the fifth and seventh ones, in the prototype PMSM. As a consequence, harmful low-frequency armature current harmonics will be effectively mitigated in the experimental drive system. Since the SVPWM switching frequency for the prototype drive system is 6kHz, the frequencies of the first and second sideband components will reach up to near 6kHz and 12kHz, respectively. Electromagnetic vibration and acoustic noise for such high frequency as 12kHz are beyond the recommended measurement upper limit of the accelerometer. Moreover, the human ear is not very sensitive to such high frequency acoustic noise so that only the first sideband components for the proposed prototype integral-slot PMSM drive system are investigated in this paper.

The experiment test on the prototype integral-slot PMSM drive system are first carried out at operational speed of 1000rpm without load, followed by a 10N·m load from the dynamometer. Due to the friction of the mechanical transmission and dynamometer, there is still noticeable load of nearly 1.2N·m under no-load condition. The phase current waveforms with 0N·m and 10N·m load from the dynamometer are captured and compared in Fig. 3(a), while the corresponding spectra at the first carrier frequency domain are compiled and illustrated in Fig. 3(b). Although the 5^{th} and 7^{th} back EMF harmonic components have been minimized by the winding arrangement, the presences of the 11^{th} and 13^{th} ones somewhat induce respective armature current harmonics and evidently distort the waveforms in Fig. 3(a). However, the armature reactions associated with these harmonics are quite small and hardly affect the modulation ratio and torque angle during steady-state operation. The speed ripple of the prototype drive is well confined within $\pm$1rpm during the experiment. Therefore, the influences of these current harmonics on the sideband current harmonics and their associated electromagnetic vibration can be neglected. Moreover, Fig. 3(b) provides the evidence of first sideband current harmonic components, and well validates that the $(\omega_s \pm 2\omega_1)$, and $(\omega_s \pm 4\omega_1)$-order current harmonic components are the main ones near the first carrier frequency. With the MTPA control algorithm, the modulation ratio with 10N·m load is nearly the same as one with no load condition and changes slightly from 0.769 to 0.789. Meanwhile, the torque angle is adjusted from about 0 to 22 degrees. It can be easily observed from Fig. 3(b) that the sideband harmonic components at first carrier frequency domain have exactly the same frequencies for both conditions. The negligible variation on modulation ratio but significant increase on torque angle make the sideband current harmonic components decline slightly under 10N·m load condition.

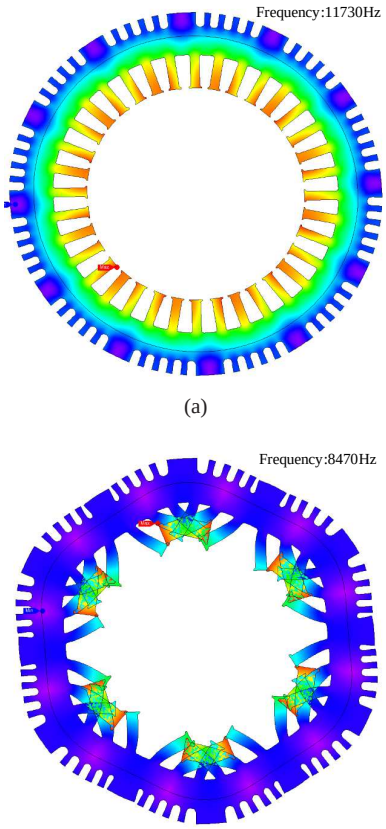

Fig. 4. 0^{th} and $2p^{th}$ vibration modes of the stator system from mechanical modal analysis: (a) 0^{th} spatial order, (b) $2p^{th}$ spatial order.

From the analytical derivations, those sideband current components will generate corresponding 0^{th} and $2p^{th}$ spatial order sideband radial electromagnetic force density components on the stator by interacting with the main low-frequency magnetic fields, and hence lead to sideband electromagnetic vibration and undesirable high-frequency acoustic noise. The natural frequencies of 0^{th} and $2p^{th}$ spatial order modes for the stator system are essential to analytically evaluate the respective electromagnetic vibration. Consequently, two-dimensional (2-D) structural FEA model together with an eigenvalue subroutine is employed to get the corresponding natural frequencies of the 0^{th} and $2p^{th}$ spatial order modes. When the eigenvalues of these modes are around the carrier frequency, serious sideband electromagnetic vibration and acoustic noise will potentially occur. The two mode shapes and their natural frequencies are obtained and illustrated in Fig. 4, which reveals 11730Hz and 8470Hz for 0^{th} and $2p^{th}$ spatial order modes respectively. There are usually distant deviations between the switching frequency and those natural ones to avoid potential resonances. However, distinctive audible noise can still be generated even though the carrier frequency is far away from the natural ones.

Furthermore, an accelerometer is attached to the centre of the machine case surface along the axial direction, as shown in Fig. 2, for the measurement of the stator vibration. The stator vibrations of the prototype PMSM at 1000rpm with

This article has been accepted for publication in a future issue of this journal, but has not been fully edited. Content may change prior to final publication. Citation information: DOI 10.1109/TPEL.2016.2602944, IEEE Transactions on Power Electronics

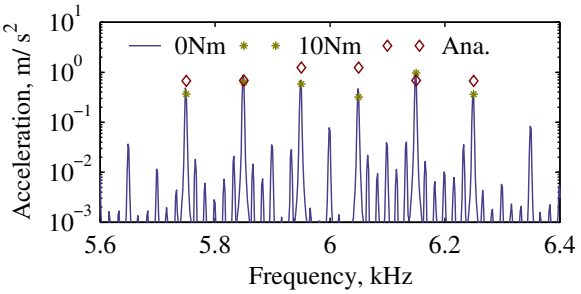

Fig. 5. Stator system vibration spectrum near the first carrier frequency at 1000rpm with no-load condition.

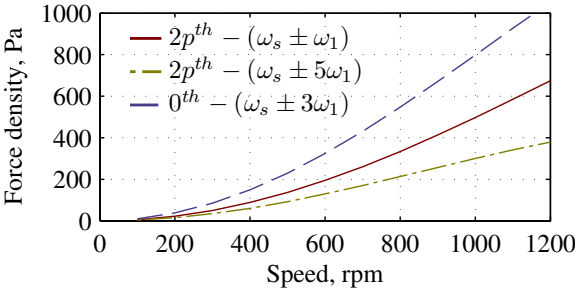

Fig. 6. Sideband radial electromagnetic force density components in the prototype drive under no load conditions with different speeds.

0N·m and 10N·m load from the dynamometer are captured and the corresponding spectra near the first carrier frequency domain is then compiled and compared with the analytical ones from (37) in Fig. 5, which clearly shows the vibrations occurring at frequencies of 5950Hz/6050Hz, 5850Hz/6150Hz, and 5750Hz/6250Hz, which are the $(\omega_s \pm \omega_1)$, $(\omega_s \pm 3\omega_1)$, and $(\omega_s \pm 5\omega_1)$ respectively. The results validate those are the main sideband electromagnetic vibration components in the first carrier frequency domain. Although the natural frequency of 0^{th} spatial order mode is much larger, the vibrations associated with the 0^{th} spatial order ones with frequencies of 5850Hz/6150Hz are very close to the $2p^{th}$ ones due to their larger radial electromagnetic force density amplitudes. However, the analytical results apparently overestimate sideband electromagnetic vibrations, as observed from Fig. 5. This is mainly due to the fact that the damping factor in the analytical calculation from empirical equation (39) are much smaller than the actual one. However, the employment of the empirical damping factor result will not lose the generality of the proposed analytical method, as it allows quick analytical evaluation without any experimental tests.

The prototype PMSM with interior PM configuration will be in severe magnetic saturation under some extremely heavy load conditions. The magnetic saturation will reduce the inductances values and introduce cross-coupling effect and hence increase the sideband current harmonics significantly [30]. However, the relevant parameters σ_1 and σ_2 given in (30) are almost immune to load and magnetic saturation for integral-slot PMSM. Therefore, the impact of magnetic saturation on the sideband radial electromagnetic force density components is very trivial and negligible. However, the load will increase the fundamental armature current component and hence the

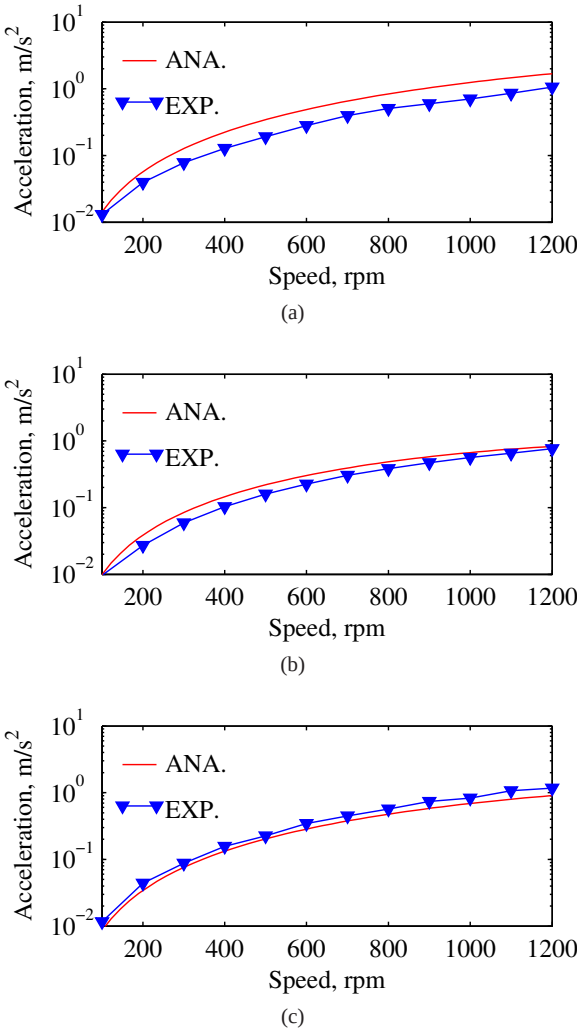

Fig. 7. Machine vibration experimental validation with no load condition at different speeds: (a) $2p^{th}$-$(\omega_s \pm \omega_1)$, (b) $2p^{th}$-$(\omega_s \pm 5\omega_1)$, (c) 0^{th}-$(\omega_s \pm 3\omega_1)$.

associated low-frequency armature reaction air-gap magnetic field. That may require a rise on the modulation ratio. Moreover, the torque angle, which has a mild effect on the sideband radial electromagnetic force density components from (34)-(36), will be adjusted under load conditions. As expected from the analytical models, the amplitudes of the main sideband electromagnetic vibration components are very close between results of 0N·m and 10N·m load from the dynamometer in Fig. 5, as modulation ratios are nearly identical. Therefore, the influence of torque angle on sideband radial force can be somewhat neglected, and the simplified analytical models in (37) are by and large valid for sideband electromagnetic vibration analysis of integral-slot PMSM in most cases. Both the analytical models and experimental tests have revealed that the impact of the torque load on the sideband electromagnetic vibration is very trivial.

B. Electromagnetic Vibration with Different Speed Conditions

From the analytical models, the sideband current harmonic components and hence the associated sideband radial electromagnetic force density ones are mainly determined by the

This article has been accepted for publication in a future issue of this journal, but has not been fully edited. Content may change prior to final publication. Citation information: DOI 10.1109/TPEL.2016.2602944, IEEE Transactions on Power Electronics

modulation ratio and torque angle. Furthermore, it can be inspected from (37) that the sideband radial electromagnetic force density amplitudes are rather independent of the torque angle for integral-slot PMSM. As the prototype integral-slot PMSM is operated with no load condition (albeit involving small friction load), the modulation ratio of SVPWM is approximately proportional to the machine rotational speed. Therefore, the amplitudes of the sideband radial electromagnetic force density components in the prototype drive with no load conditions with different speed ranged from 0 to 1200rpm are evaluated based on the analytical models and depicted in Fig. 6. The characteristics of those three sideband radial electromagnetic force density components generally comport well with the ones of the corresponding current components. As expected, the amplitudes of all three components will gradually increase as the rotational speed and hence modulation ratio rise. It can be seen from the figure that the 0^{th} spatial order ones with frequencies of $(\omega_s \pm 3\omega_1)$ are largest ones among the three, while $(\omega_s \pm \omega_1)$ ones are generally larger than the $(\omega_s \pm 5\omega_1)$ ones for the $2p^{th}$ spatial order components.

In order to validate the analytical models quantitatively, the amplitudes of the corresponding electromagnetic vibration components can be analytically evaluated by (38) with the results in Fig. 7. Moreover, comprehensive experimental tests are carried out to capture the stator vibrations of the machine with no load condition at different speeds. The corresponding amplitudes of the main vibration components in first carrier frequency domain are derived by taking the mean value of the amplitudes from five experimental samples in order to minimize the test error. The amplitudes of the $2p^{th}$ spatial order components with frequencies of $(\omega_s \pm \omega_1)$ and $(\omega_s \pm 5\omega_1)$, are compiled and compared with the analytical counterparts in Fig. 7(a) and Fig. 7(b), respectively. Whilst, the ones of 0^{th} spatial order components with frequencies of $(\omega_s \pm 3\omega_1)$ are obtained and compared in Fig. 7(c). There are notable deviations between the analytical and experimental results in Fig. 7, which reveals that the analytical models overestimate the $2p^{th}$ spatial order components but slightly underestimate the 0^{th} ones. However, the analytical results have demonstrated the tendency of the sideband electromagnetic vibration versus machine speed (modulation ratio) successfully. The analytical derivations of the sideband current harmonic components and the associated sideband radial electromagnetic force density components do not take into account the impacts of other harmonics and magnetic saturation in the machine, which are unavoidable in the prototype machine with interior PM configuration. Meanwhile, the analytical equation, which is employed to evaluate the vibration amplitude, neglects the influence of actual complex geometry of the stator. Moreover, the natural frequencies of the 0^{th} and $2p^{th}$ spatial order vibration modes are obtained from 2-D FEA, which ignores the axial effects and the impact of the phase windings. More importantly, the modal damping ratios are estimated based on the low-fidelity empirical formula which will potentially introduce considerable error. On the other hand, there are always some inevitable experimental errors. By allowing for all these factors, it is reasonable to conclude that experimental results are in satisfactory agreements with the analytical ones.

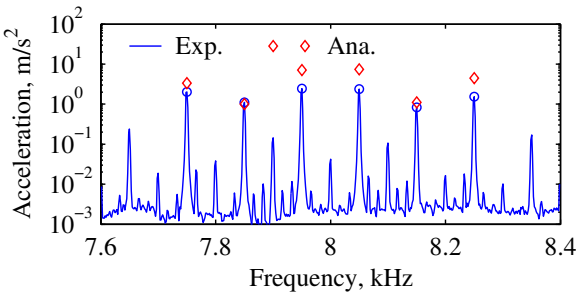

Fig. 8. Stator system vibration spectrum near the first carrier frequency at 1000rpm with no load condition and switching frequency of 8kHz.

C. Influence of Switching Frequency

As the natural frequency of $2p^{th}$ spatial order mode for the stator system of the prototype PMSM is close to 8kHz from the 2-D FEA estimation, the stator can be potentially resonating and large sideband electromagnetic vibration is expected with the switching frequency of 8kHz. The experiment test on the prototype integral-slot PMSM drive system are carried out at operational speed of 1000rpm and no load condition with switching frequency of 8kHz. Fig. 8 depicts the corresponding stator system vibration spectrum near the first carrier frequency. The comparison between Fig. 5 and 8 reveals that the $2p^{th}$ spatial order components with frequencies of $(\omega_s \pm \omega_1)$, and $(\omega_s \pm 5\omega_1)$ are significantly aggravated by the resonating phenomenon at 8kHz, while the 0^{th} spatial order ones with frequencies of $(\omega_s \pm 3\omega_1)$ keep nearly the same as the natural frequency of 0^{th} spatial order mode are far away from 8kHz. Consequently, it is always of particular importance to keep the switching frequency far away from the natural ones of the main spatial order modes so that potential resonance for sideband radial electromagnetic force can be effectively avoided. Otherwise, severe ear-piercing and unpleasant acoustic noise is more likely to be produced by the sideband harmonic components.

VI. Conclusion

Analytical investigations of the sideband radial electromagnetic force density components and the associated sideband electromagnetic vibration in integral-slot PMSM powered by VSI with regular sampled SVPWM technique have been comprehensively carried out. The critical magnetic field components from low-frequency main and high-frequency sideband magnetic field responsible for sideband electromagnetic vibration are discussed and identified. The analytical expressions of the sideband current harmonics in the first frequency domain are employed to develop the main sideband radial electromagnetic force density components and electromagnetic vibration in analytical models. Furthermore, the experimental tests on a proposed integral-slot PMSM drive system are competently undertaken to validate the new derivations. The proposed analytical models not only can be employed to predict the sideband electromagnetic vibration, but also can serve as an effective tool during the design and optimisation

stages for the machine, the power converter and the control algorithms. Moreover, the analysis approach presented can be easily adapted and applied to further studies of radial force density in other drive systems.

APPENDIX

The parameters C_{12} and C_{14} in equations (25) are determined by

$$\begin{aligned} C_{12} \approx & \frac{4}{\pi}(J_2(\frac{M\pi}{2})J_0(\frac{M\pi\xi}{2}) - J_1(\frac{M\pi}{2})J_1(\frac{M\pi\xi}{2})) \\ C_{14} \approx & \frac{4}{\pi}J_1(\frac{M\pi}{2})J_1(\frac{M\pi\xi}{2}) \end{aligned} \tag{40}$$

where

$$M \in [0, 2/\sqrt{3}], \xi = \frac{3\sqrt{3}}{8\pi} \tag{41}$$

and the k^{th} order Bessel formula can be expressed as

$$J_k(x) = \sum_{n=0}^{\infty} \frac{(-1)^n}{n!} \frac{1}{\Gamma(k+n+1)} (\frac{x}{2})^{2n+k} \tag{42}$$

where

$$\Gamma(k+n+1) = (k+n)! \tag{43}$$

REFERENCES

[1] T. M. Jahns and V. Blasko, "Recent advances in power electronics technology for industrial and traction machine drives," *Proc. IEEE*, vol. 89, no. 6, pp. 963–975, Jun. 2001.

[2] D. G. Dorrell, M. Hsieh, M. Popescu, L. Evans, D. A. Staton, and V. Grout, "A review of the design issues and techniques for radial-flux brushless surface and internal rare-earth permanent-magnet motors," *IEEE Trans. Ind. Electron.*, vol. 58, no. 9, pp. 3741–3757, Sep. 2011.

[3] L. J. Wu, Z. Q. Zhu, D. A. Staton, M. Popescu, and D. Hawkins, "Comparison of analytical models of cogging torque in surface-mounted PM machines," *IEEE Trans. Ind. Electron.*, vol. 59, no. 6, pp. 2414–2425, Jun. 2012.

[4] W. Fei and P. C. K. Luk, "A new technique of cogging torque suppression in direct-drive permanent-magnet brushless machines," *IEEE Trans. Ind. Appl.*, vol. 46, no. 4, pp. 1332–1340, Jul./Aug. 2010.

[5] ——, "Torque ripple reduction of a direct-drive permanent-magnet synchronous machine by material-efficient axial pole pairing," *IEEE Trans. Ind. Electron.*, vol. 59, no. 6, pp. 2601–2611, Jun. 2012.

[6] M. S. Islam, S. Mir, T. Sebastian, and S. Underwood, "Design considerations of sinusoidally excited permanent-magnet machines for low-torque-ripple applications," *IEEE Trans. Ind. Appl.*, vol. 41, no. 4, pp. 955–962, Jul./Aug. 2005.

[7] R. Islam, I. Husain, A. Fardoun, and K. McLaughlin, "Permanent-magnet synchronous motor magnet designs with skewing for torque ripple and cogging torque reduction," *IEEE Trans. Ind. Appl.*, vol. 45, no. 1, pp. 152–160, Jan./Feb. 2009.

[8] J. Sopanen, V. Ruuskanen, J. Nerg, and J. Pyrhonen, "Dynamic torque analysis of a wind turbine drive train including a direct-driven permanent-magnet generator," *IEEE Trans. Ind. Electron.*, vol. 58, no. 9, pp. 3859–3867, Sep. 2011.

[9] J. H. Leong and Z. Q. Zhu, "A novel torsional excitation scheme for determining mechanical transfer function and natural frequencies of circumferential vibration in pm brushless machine drives," *IEEE Trans. Magn.*, vol. 47, no. 10, pp. 4195–4198, Oct. 2011.

[10] P. Beccue, J. Neely, S. Pekarek, and D. Stutts, "Measurement and control of torque ripple-induced frame torsional vibration in a surface mount permanent magnet machine," *IEEE Trans. Power Electron.*, vol. 20, no. 1, pp. 182–191, Jan. 2005.

[11] W. Zhu, S. Pekarek, B. Fahimi, and B. J. Deken, "Investigation of force generation in a permanent magnet synchronous machine," *IEEE Trans. Energy Convers.*, vol. 22, no. 3, pp. 557–565, Sep. 2007.

[12] Z. Q. Zhu, Z. P. Xia, L. J. Wu, and G. W. Jewell, "Analytical modeling and finite-element computation of radial vibration force in fractional-slot permanent-magnet brushless machines," *IEEE Trans. Ind. Appl.*, vol. 46, no. 5, pp. 1908–1918, Sep./Oct. 2010.

[13] G. Dajaku and D. Gerling, "The influence of permeance effect on the magnetic radial forces of permanent magnet synchronous machines," *IEEE Trans. Magn.*, vol. 49, no. 6, pp. 2953–2966, Jun. 2013.

[14] M. Valavi, A. Nysveen, and R. Nilssen, "Effects of loading and slot harmonic on radial magnetic forces in low-speed permanent magnet machine with concentrated windings," *IEEE Trans. Magn.*, vol. 51, no. 6, pp. 1–10, Jun. 2015.

[15] R. Islam and I. Husain, "Analytical model for predicting noise and vibration in permanent-magnet synchronous motors," *IEEE Trans. Ind. Appl.*, vol. 46, no. 6, pp. 2346–2354, Nov./Dec. 2010.

[16] M. S. Islam, R. Islam, and T. Sebastian, "Noise and vibration characteristics of permanent-magnet synchronous motors using electromagnetic and structural analyses," *IEEE Trans. Ind. Appl.*, vol. 50, no. 5, pp. 3214–3222, Sep./Oct. 2014.

[17] D. Torregrossa, F. Peyraut, B. Fahimi, J. MBoua, and A. Miraoui, "Multiphysics finite-element modeling for vibration and acoustic analysis of permanent magnet synchronous machine," *IEEE Trans. Energy Convers.*, vol. 26, no. 2, pp. 490–500, Jun. 2011.

[18] A. Ruiz-Gonzlez, M. J. Meco-Gutirrez, F. Prez-Hidalgo, F. Vargas-Merino, and J. R. Heredia-Larrubia, "Reducing acoustic noise radiated by inverter-fed induction motors controlled by a new PWM strategy," *IEEE Trans. Ind. Electron.*, vol. 57, no. 1, pp. 228–236, Jan. 2010.

[19] A. Ruiz-Gonzlez, F. Vargas-Merino, F. Perez-Hidalgo, M. J. Meco-Gutierrez, and J. R. Heredia-Larrubia, "Low switching PWM strategy to reduce acoustic noise radiated by inverter-fed induction motors," in *Proc. IEEE Int. Symp. Ind. Electron.*, Jul. 2010, pp. 1353–1358.

[20] A. Ruiz-Gonzlez, F. Vargas-Merino, J. R. Heredia-Larrubia, M. J. Meco-Gutierrez, and F. Perez-Hidalgo, "Application of slope PWM strategies to reduce acoustic noise radiated by inverter-fed induction motors," *IEEE Trans. Ind. Electron.*, vol. 60, no. 7, pp. 2555–2563, Jul. 2013.

[21] C. M. Liaw, Y. M. Lin, C. H. Wu, and K. I. Hwu, "Analysis, design, and implementation of a random frequency PWM inverter," *IEEE Trans. Power Electron.*, vol. 15, no. 5, pp. 843–854, Sep. 2000.

[22] A. Peyghambari, A. Dastfan, and A. Ahmadyfard, "Selective voltage noise cancellation in three-phase inverter using random SVPWM," *IEEE Trans. Power Electron.*, vol. 31, no. 6, pp. 4604–4610, June 2016.

[23] J. Le Besnerais, V. Lanfranchi, M. Hecquet, and P. Brochet, "Characterization and reduction of audible magnetic noise due to PWM supply in induction machines," *IEEE Trans. Ind. Electron.*, vol. 57, no. 4, pp. 1288–1295, Apr. 2010.

[24] J. A. Ferreira, P. Dorland, and F. G. de Beer, "An active inline notch filter for reducing acoustic noise in drives," *IEEE Trans. Ind. Appl.*, vol. 43, no. 3, pp. 798–804, May/Jun. 2007.

[25] W. Liang, J. Wang, and W. Fang, "Analytical modeling of sideband current harmonic components in induction machine drive with voltage source inverter by an SVM technique," *IEEE Trans. Power Electron.*, vol. 28, no. 11, pp. 5372–5379, Nov. 2013.

[26] W. Liang, J. Wang, P. C. K. Luk, W. Fang, and W. Fei, "Analytical modeling of current harmonic components in PMSM drive with voltage-source inverter by SVPWM technique," *IEEE Trans. Energy Convers.*, vol. 29, no. 3, pp. 673–680, Sep. 2014.

[27] J. F. Gieras, C. Wang, and J. C. Lai, *Noise of Polyphase Electric Motors*, ser. Electrical and Computer Engineering. CRC Press, 2005.

[28] S. J. Yang, *Low-Noise Electrical Motors*, ser. Monographs in Electrical and Electronic Engineering. Oxford University Press, 1981.

[29] R. Krishnan, *Electric Motor Drives: Modeling, Analysis, and Control*. Prentice Hall, 2001.

[30] W. Liang, W. Fei, and P. C. K. Luk, "An improved sideband current harmonic model of interior pmsm drive by considering magnetic saturation and cross-coupling effects," *IEEE Trans. Ind. Electron.*, vol. 63, no. 7, pp. 4097–4104, Jul. 2016.

This article has been accepted for publication in a future issue of this journal, but has not been fully edited. Content may change prior to final publication. Citation information: DOI 10.1109/TPEL.2016.2602944, IEEE Transactions on Power Electronics

Wenyi Liang was born in Zhejiang, China, 1982. He received the B.Eng. and M.Eng. degrees in electrical engineering from Zhejiang University, Hangzhou, China, in 2004 and 2006, respectively.

From 2006 to 2014, he was a Development Engineer in Hangzhou Easitech Corporation, Hangzhou. He is currently a Research Fellow with the Power Engineering Centre, Cranfield University, Cranfield, U.K. His current research interests include design, analysis, and applications of electric machines and drives.

Patrick Chi-Kwong Luk (M'92-SM'08) was born in Hong Kong. He received the High Diploma with merits (B.Sc) in electrical engineering from Hong Kong Polytechnic University, Hung Hom, Kowloon, Hong Kong, in 1983, the M.Phil. Degree in electrical engineering from Sheffield University, Sheffield, U.K., in 1989, and the Ph.D. degree in electrical engineering from the University of South Wales, U.K., in 1992.

He started his career in industry as Engineer Trainee between 1981 and 1983 at GEC (H.K.) and then after graduation as Applications Engineer at Polytek Engineering Co. (H.K.) In 1986, he worked as Senior Researcher in the Industrial Centre at PolyU. Since 1988, he had held academic positions at the University of South Wales, Robert Gordon University, Aberdeen, U.K., and the University of Hertfordshire, U.K. He joined Cranfield University, Bedford, U.K., in 2002, where he is a Chair Professor in electrical engineering and Head of the Electric Power and Drives Group, Power Engineering Centre. He has held chair positions in the IEEE UK&I Power Electronics/Industrial Electronics Chapters, and is currently Chair for IEEE UK&I Professional Communications. He has authored more than 170 publications in electric machines, power electronics and energy conversion systems. His current research interests include electrical drives, renewable energy systems, and high-frequency power electronics.

Weizhong Fei (M'12) was born in Zhejiang, China, 1981. He received the B.Eng. and M.Eng. degrees from Zhejiang University, Hangzhou, China, in 2004 and 2006, respectively, and the Ph.D. degree from Cranfield University, Shrivenham, U.K., in 2010, all in electrical engineering.

From 2011 to 2012, he was a Research Associate at the University of Sheffield, Sheffield, U.K. Since 2012, he has been with Cranfield University, Cranfield, U.K. where he is currently a Lecturer in Clean Energy Technology. His current research interests include design and applications of high efficient energy conversion systems.